Development of Small-Scale Monitoring and Modeling Strategies for Safe Lithium-Ion Batteries

Yawen Zhang,[a] Peng Chen,[a] Tianyi Wang,*[a] Dawei Su,*[b] and Chengyin Wang[a]

Batteries & Supercaps

Review
doi.org/10.1002/batt.202100292

Chemistry
Europe
European Chemical
Societies Publishing

Lithium-ion batteries (LIBs) have the advantages of high energy density, stable working voltage, long cycling life, and no memory effect. They have been widely used as power sources for electric vehicles (EVs) and hybrid electric vehicles (HEVs). However, during periods of usage or storage, some unfavorable factors such as thermal runaway, volumetric expansion, and growth of lithium dendrites can severely reduce the reliability and safety of LIBs. Therefore, an accurate health estimation system and a reliable life expectancy strategy toward LIBs have been proved significantly important. However, due to the large volume and high price, most characterization methods in the laboratory cannot be applied directly to commercial electric devices. Therefore, small portable monitor methods are more practical. In this review, we first systematically reviewed the recent progress of modeling methods towards LIBs. Some typical modeling strategies (e.g., thermal models, electrical models and aging models) and advanced sensors which can be imbedded in LIBs are emphatically introduced and compared. At last, some promising directions of development on portable in-situ monitor strategies are also predicted and supposed.

1. Introduction

Compared with other secondary batteries, lithium-ion batteries (LIBs) have the advantages of high energy density, low toxicity, high working voltage, long cycle life, and no memory effects.[1] In 1980, J. B. Goodenough firstly introduced Li_xCoO_2 as a cathode material to realize the working of LIBs. This breakthrough usher our lives into the era of portable electronic devices. In 1991, Sony Corporation of Japan launched the world's first commercial LIBs with carbon materials as negative electrodes and lithium-containing metal oxides as positive electrodes, which also realize the commercialization of LIBs.[2] With the prosperous development and quick promotion of clean, renewable, and distributed energy technologies globally, LIBs have been widely used as the fundamental power source for electric vehicles and portable electronic devices. The global market value of LIBs is multiplying every year which is shown by the statistics from 2011 to 2020 in Figure 1(a).[2]

However, during the working or storage periods, some adverse issues can severely reduce the reliability and safety of LIBs.[3] i) The lithium metal anode, which has been widely regarded as a promising anode candidate for high energy density LIBs, is still suffering from some unfavorable issues, such as uncontrollable growth of Li dendrites and instability of solid electrolyte interphases (SEI) layer. Once dendrites penetrate the separator, the direct contact between anodes and cathode normally result in short circuit, which will cause thermal runaway or even explosion of whole batteries.[4] ii) During the charging/discharging cycles, the large volumetric expansion ratio normally affects the fragile integrity of electrodes. A larger volumetric expansion can result in the collapse of the structure of active materials on both cathodes and anodes,

which can cause quick decrease of capacity of batteries.[5] iii) Accompanied with charging/discharging processes of batteries, the fragmentation/recovering process of SEI layers can not only thicken the SEI layer, cause the loss of electrolyte and active material, but also increase the internal electrochemical impedance of batteries.[6] iv) Some other issues, such as the rise of internal temperature of batteries, the gas released from decomposition of electrolyte can also affect the working states of batteries and risk the safety of their users.[7] Therefore, it is particularly important to monitor the health of LIBs in real time. Through real-time monitoring of the internal state of the battery, analysis of its electrochemical reaction, and possible failure causes, the endogenous events of the battery can be observed. Early warning and health management strategies for batteries have been taken into consideration of the design of next generation high energy density LIBs.

To date, most in-situ characterization methods such as in-situ scanning electron microscope (SEM),[8] in-situ atomic force microscope (AFM),[9] in-situ nuclear magnetic resonance (NMR)[10] and in-situ transmission electron microscope (TEM) have been commonly used to observe the real time reaction of batteries.[11,12] However, due to their large volume and high price, these methods are not suitable for commercial applications. At the same time, with the rapid development of microelectronic techniques and modelling calculation, many small portable analytical methods such as sensors and modelling strategies are constantly emerging in the field of batteries.[13] For intelligent sensing, the earliest date can be traced back to 1887 when a hydrometer was firstly used to measure the electrolyte density in lead-acid batteries to estimate their state of charge. Since then, the field has witnessed the development of other diagnostic tools, which rely on the use of thermocouples, thermistors, pressure gauges, acoustic probes and differential thermal analysis. Recently, a large number of on-board electrochemical impedance spectroscopy have been introduced (as shown in Figure 1b).[14] For promising the safety of commercial batteries, many strategies have been widely employed: i) Big Data Early Warning System. This system can analyzes and extracts the deep features of data, and combined with signal testing and transmission technology, builds a fault real-time testing system that provides early warnings about battery faults. ii) Cell Health Examination Technology. This examination technology can be combined with the cell failure mechanism model, which support the real-

[a] Y. Zhang, P. Chen, Dr. T. Wang, Prof. C. Wang
     School of Chemistry and Chemical Engineering
     Yangzhou University
     180 Si-Wang-Ting Road
     Yangzhou, 225002, Jiangsu Province, China
     E-mail: yzwangtianyi@foxmail.com
[b] Prof. D. Su
     Center for Clean Energy Technology
     School of Mathematical and Physical Science
     Faculty of Science
     University of Technology Sydney
     Sydney, NSW 2000, Australia
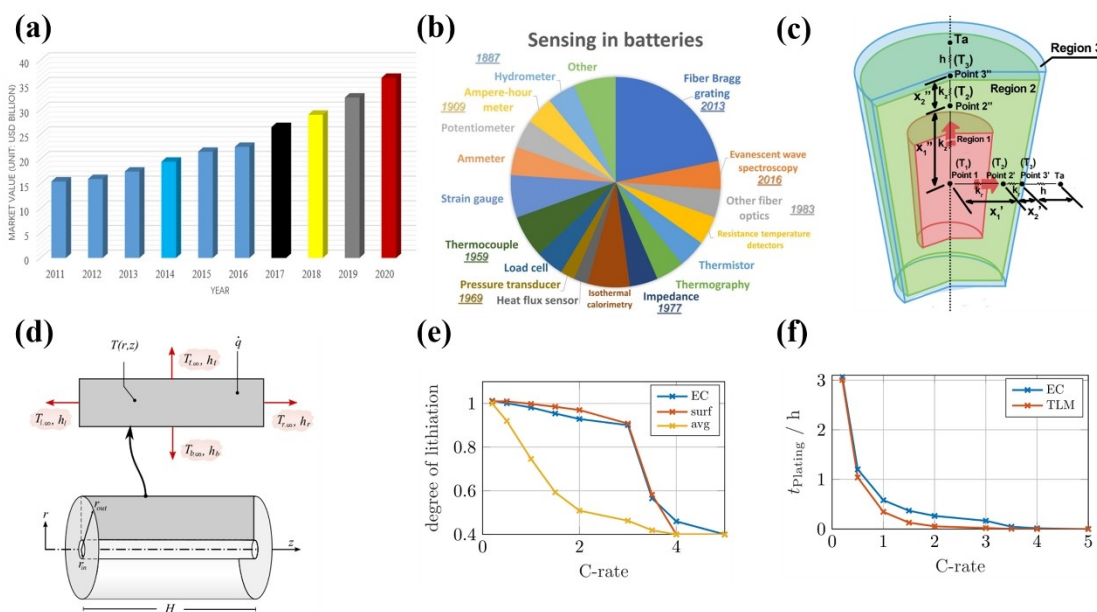   E-mail: dawei.su@uts.edu.au

Figure 1. (a) Lithium-ion batteries' world market value from 2011 to 2020. Adapted with permission from Ref. [2]. Copyright (2019) Elsevier. (b) A glance at sensing technologies in batteries. Adapted with permission from Ref. [14]. Copyright (2020) The Author(s). (c) One-dimensional thermal model of a LIB. Adapted with permission from Ref. [24]. Copyright (2020) IEEE. (d) Schematic of cylindrical cell geometry for the thermal model, showing different convection coefficients and/or external temperatures at each surface. Adapted with permission from Ref. [25]. Copyright (2016) Elsevier. (e) Simulated degree of lithiation at starting Li deposition for various C-rates for the EC model and the TLM at the particle surface of the separator-close layer and the average. (f) The corresponding charging times until beginning Li deposition. Adapted with permission from Ref. [37]. Copyright (2020) Elsevier.
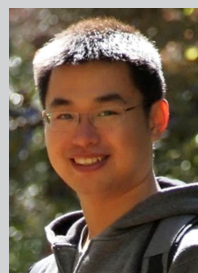
time monitors to all kinds of batteries. iii) Wireless BMS. The wireless communication technology within the pack can largely simplify the sample harness, convenient pack assembly and improve reliability of the battery to realize a long monitoring span for 24 hours.[15] In this review, some latest development of portable analytical methods for LIBs have been discussed. Some typical models and sensors are included.

2. Model-Based Methods

LIB is widely used in various energy intensive industries, such as new energy vehicles, power microgrid, aerospace and so on. The establishment of battery model is of great significance to the study of battery characteristics, SOC (state of charge) estimation, SOH (state of health) estimation, BMS (battery management system) algorithm development and fast real-time simulation of battery system.[16] In this chapter, we focus on the thermal model, electrical model and multi-coupling model.
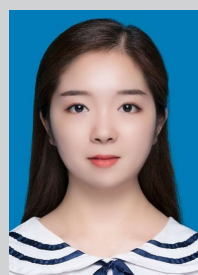
Yawen Zhang is a student currently under Professor Chengyin Wang's supervision at Yangzhou University of Chemistry, China. Her research mainly focuses on the field of the microcantilever sensor and its applications.

Chengyin Wang is currently a professor in the College of Chemistry and Chemical Engineering at Yangzhou University. His research interests focus on analytical chemistry for materials, functional materials, and electrochemical sensors.

Tianyi Wang received his Ph.D. from the Centre for Clean Energy Technology at the University of Technology Sydney (UTS), Australia. Currently, he is working in the College of Chemistry and Chemical Engineering, Yangzhou University (YZU) and devoted himself to the exploration on Li-ion batteries, Sensors, Li-S batteries, Li metal anode and biomaterials.

Dawei Su is Senior Lecturer for School of Mathematical and Physical Sciences in Faculty of Science. His original research related to advanced energy storage and conversion, His research activities involve the design, investigation, and development of novel nano-structured materials for batteries applications.

Batteries & Supercaps

Review
doi.org/10.1002/batt.202100292

Chemistry
Europe

European Chemical
Societies Publishing

2.1. Thermal Model

Temperature is an important parameter that affects battery performance for the electrodeposition of lithium is controlled by reaction thermo dynamic.[17] In 2019, Yan et al. reported that a higher working temperature can enlarge the nucleation size of Li nuclei, hence improving the Coulombic efficiency of Li metal anodes.[18] However, in 2021, Cui et al. demonstrated that a low temperature of storage is beneficial to their calendar ageing so most LIBs should be stored in a low temperature.[19] Not only that, in commercial applications such as EVs, the sudden jump of temperature is linked to the short circuit so that a real time monitoring to temperature of battery matrix has been essential important for drivers' safety.[20]

At present, most research teams at home and abroad use battery thermal model and numerical simulation finite element technology to study the thermal effect of battery module. Onda et al.[21] took Sony $LiCo_2/C$ cylindrical LIBs as the research object, established a one-dimensional thermal model along the radial direction to explore the internal temperature distribution of the battery. The thermal behavior of the battery can be displayed by measuring the over potential resistance, entropy change, thermal capacity and heat transfer coefficient with ambient air. In the process of charge and discharge, the calculation model coincides with the basic temperature curve of the test. However, for large batteries or high-rate load conditions, one dimension is not enough. Therefore, Kim et al.[22] took 14.6 Ah $LiMn_2O_4/C$ LIBs as the research object and established a two-dimensional simplified model of electrode (positive and negative). The law of charge conservation is used to describe the material transfer relationship between two electrodes and predict the thermal behavior of lithium-ion battery during charge and discharge. The two-dimensional model extends the battery temperature prediction to large batteries. In order to further improve the calculation accuracy, Du et al.[23] took 3.2 V/10 Ah LFP ($LiFePO_4$) batteries as the research object and proposed a three-dimensional thermal model considering the heat generated by the body and collector. The results show that the thermal behavior of battery discharge process can be effectively simulated by coupling the dynamic changes of battery temperature, internal resistance and temperature coefficient.

The above method improves the prediction accuracy, but the calculation is complex, so it is difficult to apply this kind of model to the on-line temperature detection of battery. In order to solve this problem, the research on simplifying three-dimensional thermal model is emerging one after another. Xie et al.[24] added internal resistance identification and SOC estimation to the temperature estimation process and proposed an improved LIB internal temperature estimation method using one-dimensional model and double Kalman filter. The thermal model of cylindrical battery is simplified to a one-dimensional thermal model with three nodes and each node is selected to balance accuracy and calculation speed. Firstly, as shown in Figure 1(c), the cylindrical battery is divided into three parts: Region 1, Region 2, and Region 3. Region 3, which is a thin coating layer, represents the external part that is

in direct contact with the environment. Region 1 represents the core bar of the battery, where the core empty part is taken into consideration, and Region 2 is the other parts of the battery. The energy transfer between the three points can be revealed according to the energy function in the heat transfer theory. Compared with the temperature field simulated by high fidelity three-dimensional model, it is proved that this method has high estimation accuracy. The experimental results show that the double Kalman filtering method has better stability than the single Kalman filtering method. By considering the equivalent thermal conductivity identification of thermal conductivity anisotropy in different directions, the accuracy of internal temperature estimation can be largely improved. Richardson et al.[25] successfully built a low-order two-dimensional thermal model of cylindrical lithium-ion battery, which can predict the omni-directional temperature distribution of the battery (Figure 1d). The accuracy of the model is verified by comparing with the finite element simulation results. The results show that the two-dimensional temperature field of large-size (64 mm diameter) battery can be accurately simulated in only four states.

In order to realize the on-line temperature detection of large LIBs, Cui et al.[26] studied 50 Ah hard shell LIBs with Nickel Cobalt Manganese (NCM) based cathode materials and graphite-based anode materials. Three lumped parameter thermal models for hard shell LIBs are proposed, including two-state lumped thermal model (2STM), five state lumped thermal model (5STM) and improved five state lumped thermal model (5STM+). 5STM+ considers heat transfer between 5STM surface states. The lumped parameter thermal model is implemented on a notebook computer equipped with 1.6 GHz eight core processor and 8G random access memory. The applicability of the model is confirmed by evaluating the calculation accuracy under seven possible applications of the battery. It is found that 5STM+ provides high calculation accuracy in all proposed cases, including natural convection, forced air convection, regional liquid cooling and local heating. At the same time, for a physical time of 1 h, the calculation time consumption of 5STM+ is milliseconds, while the physical modeling uses 12000 s at most. Therefore, 5STM+ is very effective. It can be well embedded in the microcontroller in BMS to realize the online estimation of battery internal temperature. In conclusion, the dimensionality reduction method effectively simplifies the complex three-dimensional thermal model, which provides the possibility of commercial online temperature monitoring of the battery.

In conclusion, one-dimensional thermal model can monitor the internal temperature of battery, but it is far more enough for large scale batteries or some special battery for high current density discharge/charge functions. The two-dimensional thermal model extends the battery temperature prediction to pouch batteries and is most suitable to next generation high energy density power batteries. The three-dimensional thermal model can support the most accurate information about batteries especially for large scale power batteries. However, accompanied with the improvement of dimension, the higher demanding on data processing and computing algorism makes

Batteries & Supercaps

Review
doi.org/10.1002/batt.202100292

Chemistry
Europe
European Chemical
Societies Publishing

three-dimensional model more suitable for large scale energy storage matrix (e.g., large energy storage stations) rather than small battery matrix. Therefore, the dimensionality reduction method can effectively simplify the complex three-dimensional thermal model, which provides the possibility of application for the on-line temperature monitoring of the battery.

2.2. Electrical Model

The electrical model can both respond to the macroscopic electrical parameters of batteries, shorten testing time, save testing cost and characterize microstructure of the particle to assess battery performances for meeting different requirements of various management systems. Battery electric models mainly consist of the electrochemical model, reduced-order model, equivalent circuit model, and data-driven model.[1c] Currently, most electric vehicle are employing electrochemical model (EM) and equivalent circuit model(ECM) as their main monitor methods.[27]

2.2.1. Electrochemical Model

Based on the internal electrochemical reaction mechanism of the battery, the electrochemical model can accurately predict the internal state of the battery (lithium-ion concentration, electrolyte potential, current distribution, etc.). The most common EM are single particle (SP) model and quasi two-dimensional (P2D) model.[28] The SP uses two spherical particles to replace all the active substances at the positive and negative poles of the battery and ignores the detailed distribution of lithium-ion concentration in the liquid phase. Although the amount of calculation is reduced to a certain extent, the model is only applicable to the case of low magnification.[29] P2D model is usually called quasi two-dimensional model, because in spherical particles, one dimension is x and the other dimension is radial dimension R. The P2D model regards the anode and cathode of the battery as porous electrodes composed of many spherical particles, and the space between the particles is filled with electrolyte. Several coupled partial differential equations (PDE) describe the concentration distribution and potential distribution of lithium ions in the liquid phase of electrolyte and the solid phase of electrode material particles, so as to comprehensively check the main reaction and side reaction inside the battery.[27,30] P2D model has been widely concerned and applied since its birth. Model studies shifted from single-phase materials (lithium manganese oxide [LMO][31] and lithium cobalt oxide [LCO][32]) to multiphase materials (lithium iron phosphate [LFP],[33] nickel cobalt manganese [NCM],[34] and nickel-cobalt-alumina [NCA]).[35] Although the precision of P2D model is very high, it contains a large number of partial differential equations and the coupling of state variables, which makes the calculation very complex. It is only suitable for the pre battery optimization and design and cannot be applied to the real-time battery management

system. Therefore, improving the accuracy of SP model and simplifying P2D model have become the focus of research.

Lyu et al.[36] developed a simplified EM (SEM) and parameter identification method based on SP model to realize the in-situ study of LIB aging. Firstly, the EM model is developed based on the SP model, which simplifies the symbols, names and descriptions of 10 parameters in the model (e.g., positive and negative capacity, resistance). Compared with the original SP model, the improved EM reduces the number of parameters from 17 to 10, reducing the burden of parameter identification. Then, by applying a series of specially designed current activation to the battery, the overvoltage is decoupled from the measured terminal voltage for parameter identification. Finally, 14500 $LiCoO_2$/C battery (nominal capacity 750 mAh) was used for cyclic aging test. The model parameters were identified every 10 or 20 cycles (up to 130 cycles). The experimental results show that the predicted trend of 7 of the 10 model parameters (including internal resistance) is closely related to the battery degradation.

Hahn et al.[37] proposed a discrete EM (representative with TLB) to realize the in-situ detection of local lithium plating. Discretization can explain the ongoing process and local state spatially. Figure 1€ shows the simulated degree of lithiation (DOL) when TLB and standard equivalent circuit (EC) start lithium deposition at different C-rates. When the charging current was 1 C, the DOL detected by TLM still reached the electroplating standard ≈ 1 of EC. When the charging current is 3.5 C, the transmission line (TLM) surface intersects the EC curve. Starting from 4 C, TLM predicts electroplating from the first second of charging, which is very reasonable for high-energy batteries. EC obtained the same result at 5 C. Figure 1(f) shows the expected charging time of EC and TLM without plating. The time when TLM stops charging between 0.5 C and 3 C is significantly earlier than EC, indicating that EC is not suitable for correctly predicting electroplating at high current. Therefore, TLM is more sensitive to the detection of lithium deposition than standard EC. Due to the high sensitivity of TLM and the ability to detect local lithium deposition, the TLM proposed in this study can realize the early detection of local lithium deposition. In conclusion, the simplified EM ensures the accuracy of the model under high complexity conditions and is suitable for online BMS.

2.2.2. Equivalent Circuit Model

To date, for many applications, it is essential to strike a balance between the complexity of the model and the accuracy to embed the model in the microprocessor and deliver accurate results in real time. Due to the complexity of the electrochemical model, adding resistance, capacitance, and voltage source into the circuit established an ECM. ECM is one of the most commonly useful battery modeling methods in electric vehicle applications. Common ECM include Rint model, Thevenin model, Partnership for a New Generation of Vehicles (PNGV) model and General Non-Linear (GNL) model.[27,38]

Rint model is an equivalent internal resistance model based on the internal resistance of the battery. It is the simplest ECM. The battery model consists of an ideal voltage source and a battery resistor in series. As shown in Figure 2(a), V_{oc} represents the ideal voltage source equivalent to the battery, and the resistor is represented by R_o. The V_{oc} of the battery can be obtained from the OCV-SOC curve of the battery, and the resistance Ro can be obtained by measuring the ratio of voltage and current between battery charge and discharge. In the figure, V_t is the terminal voltage of the battery and I_L is the current. As the Rint model is a simple linear equivalent model, it does not take into account the transient process in the operation of the battery and cannot better simulate the nonlinear characteristics of the battery. It can only be used in the simple simulation research of the battery but cannot study the characteristics of the battery under complex working conditions.[39] In order to further improve the accuracy of the model, an RC parallel circuit is added to the circuit of Rint model to describe the internal polarization efficiency of the battery, also known as Thevenin model (Figure 2b). This model can also be regarded as a first-order RC model, in which C_p and resistance R_p are the polarization capacitance and polarization resistance of the battery respectively. Other parameters have the same meaning as those in Rint model. The structure of the model is relatively simple, the calculation time is short, and it has good practical value. When SOH changes little, the charge and discharge behavior of LIB under constant current and constant temperature can be accurately simulated. However, as the battery ages or the temperature changes greatly, the accuracy of the model will decrease.[1a,40]

PNGV model is a derivative model of Thevenin model. A capacitor is connected in series on the main circuit of Thevenin model to describe the change of LIB open circuit voltage. GNL combines the advantages of the above four models, with wider application range, higher accuracy, the most complex structure and the largest calculation time consumption.[38b] From the above literature review, it can be seen that the simple low-order model faces the challenge of accurately describing the battery state, while the complex high-order model will greatly increase the difficulty of model parameter calculation and identification. Therefore, a large number of researchers have improved ECM to obtain more accurate SOC estimation.

Wu et al.[41] introduced an Unsymmetrical Thevenin (UT) model to obtain more accurate state of charge (SOC) estimation. The structure of UT model is shown in Figure 2(c). The model consists of voltage source, asymmetric equivalent series resistance and polarization voltage. The voltage source is also called open circuit voltage (OCV) of power LIB. When the battery is under load, the terminal voltage drops below OCV, and when the battery is charged, the terminal voltage rises above. The equivalent series resistance during charging is different from that during discharging, which is the main difference from the traditional Thevenin model. Polarization voltage means that the deviation between terminal voltage and OCV develops slowly with the passage of time. The polarization resistance and capacitance during charging are also different from those during discharge. In addition, Auto-tuning Multiple Forgetting Factors Recursive Least Squares (AMFFRLS) is proposed for model parameter identification. Adaptive Time Scale Dual Extend Kalman Filtering (ATSDEKF) to update the model parameters. The experimental results of INR 18650-20R battery show that the model parameter identification method can obtain a more accurate model than the classical Forgetting Factors Recursive Least (FFRL) method. In terms of SOC estimation, the method proposed by the model obtains better SOC estimation results than Extend Kalman Filtering (EKF) with fixed model parameters under different working conditions and temperatures. The predicted root
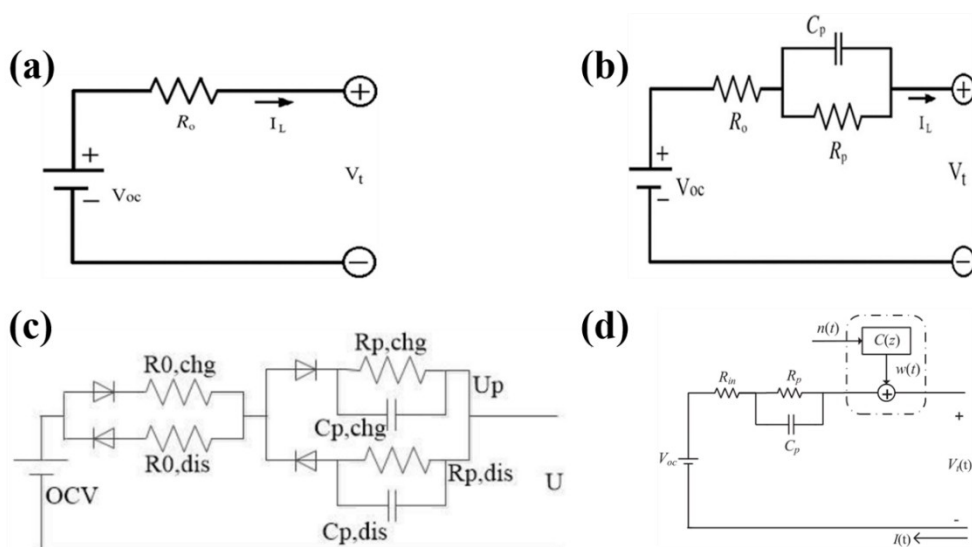

Figure 2. (a) Rint model. (b) One RC network battery model (Thevenin model). Adapted with permission from Ref. [1a]. Copyright (2015) Elsevier. (c) Structure of UT model. Adapted with permission from Ref. [41]. Copyright (2021) Elsevier. (d) Proposed equivalent-circuit model. Adapted with permission from Ref. [13b]. Copyright (2015) Elsevier.

Batteries & Supercaps

Review
doi.org/10.1002/batt.202100292

Chemistry Europe
European Chemical
Societies Publishing

means square error (RMSE) of terminal voltage is basically lower than 1 mV, and the estimated RMSE of SOC is less than 0.12.

Feng et al.[13b] proposed an improved ECM to simulate the dynamic characteristics of the battery. The error of RC circuit is compensated by adding moving average (MA) noise to the single resistance capacitance (RC) circuit model. It can accurately capture battery dynamics and maintain a simple topology. As shown in Figure 2(d), the proposed ECM is based on an RC circuit and adds colored noise $w(t)$ on the output side of the model. Controllable voltage source V_{oc} is used to describe the open circuit voltage of the battery. R_{in} is an ohmic resistor that simulates the electrolyte resistance and connection resistance of the battery. RC circuit is used to simulate the charge transfer phenomenon of battery. $w(t)$ covers other battery dynamics not considered in an RC circuit model, such as diffusion. In practical application, $w(t)$ is updated by the last measured data of battery current and voltage, so as to simulate the real battery dynamics. $V_t(t)$ and $I(t)$ are the terminal voltage and current of the battery respectively. The parameters of the proposed ECM are identified online by Recursive Extended Least Squares (RELS). In the dynamic test experiment of battery, the improved ECM and single RC circuit can realize the dynamic unbiased simulation of battery. However, compared with the single RC circuit model, the error of the improved ECM is significantly reduced. The maximum output error of an RC circuit is as high as 146 mV, while the maximum output error of the improved ECM is only 19 mV.

To sum up, the Rint model does not take into account the transient process in the operation of the battery and cannot better simulate the nonlinear characteristics of the battery, so it can only be used in the simple simulation study of the battery; Although the Thevenin model has short calculation time and high accuracy, it is only suitable for the case of little change in SOH. The improved electrochemical model increases the application range and can realize the dynamic unbiased simulation of the battery, which is suitable for the on-line battery management system.

2.3. Multiphysics Modeling

The individual thermal or electrical properties are not enough to characterize all the battery features. As a closed system, it is necessary to combine various physical characteristics together. In principle, three main physical parameters (electrical, thermal and mechanical properties) should be taken into consideration.[42] In this chapter, we mainly focus on thermal-electrochemical model, thermal-equivalent circuit, thermal-electricity-aging model and thermo-electric-mechanical model.

2.3.1. Thermal-Electrochemical Coupled Model

The battery temperature will affect the battery parameters (such as resistance), thus changing the battery voltage characteristics. Generally speaking, the higher the temperature, the smaller the internal resistance, and the lower the battery

voltage relative to the load current. To capture the electrical components (such as current, voltage, SOC) and thermal features (such as surface and internal temperature) of the battery, the establishment of an electrochemical-thermal coupling model can fully reflect the EC—T behavior of the cell under different operating conditions.[1c,27] The electrochemical model can be linked to the thermal model through Arrhenius law [Eq. (1)], which gives the relationship between transport and kinetic parameters Ψ and temperature T.

$$\psi = \psi_{ref} \cdot \exp\left[\frac{E_a(\psi)}{R}\left(\frac{1}{T_{ref}} - \frac{1}{T}\right)\right] \tag{1}$$

Farag et al.[43] took the large prismatic battery as the research object and established a model combining electro-chemistry, heat generation and thermology to accurately predict the terminal voltage and core temperature of the battery. The heating model considers three heat sources (irreversible loss, reversible loss and mixed heat) during operation. The effectiveness of the combined model is verified under different current rates (0–12 C) and temperature ranges (−25 °C to 45 °C). The results show that the proposed model not only maintains a simple mathematical structure, but also displays accurate terminal voltage (RSME = 0.039) and core temperature prediction (RSME < 1.134) under various operating conditions, making it an ideal choice for real-time BMS applications.

As shown in Figure 3(a), Gao et al.[44] proposed a simplified electrochemical thermal model and successfully applied it to EV BMS. Firstly, the P2D model is simplified by Laplace transform to obtain the transfer function EM. Then, the reduced order model is extended with the Arrhenius relation [Eq. (1)] of the model parameters to consider the temperature change. The 1 C full discharge and Urban Dynamometer Driving Schedule (UDDS) curves in the temperature range of −10 °C to 30 °C were used to verify the effectiveness of the model. When the temperature drops to −10 °C, the RMSE of the predicted voltage is less than 28 mV. Finally, the EM is discretized and integrated into the electric vehicle BMS. The model is verified by four improved Common Artemis Driving Cycle Urban (CADC) where the RMSE of online voltage is less than 15.8 mV, indicating that the developed model can be used in a wider range of electric vehicle applications.

2.3.2. Thermal-Equivalent Circuit Coupled Model

ECM is used as the electrical characteristic model, and a thermal model is coupled to simulate the electrothermal response of LIB. This model is relatively simple and easy to be popularized in real vehicles. Jiang et al.[45] developed a low computational electrothermal coupling model. The new model provides a promising candidate for developing rapid charging and internal heating strategies and stimulating power batteries in cold weather.

In addition, Pan et al.[46] proposed a pseudo 3D multi-node electrical thermal model (MNETM) considering the shell interval
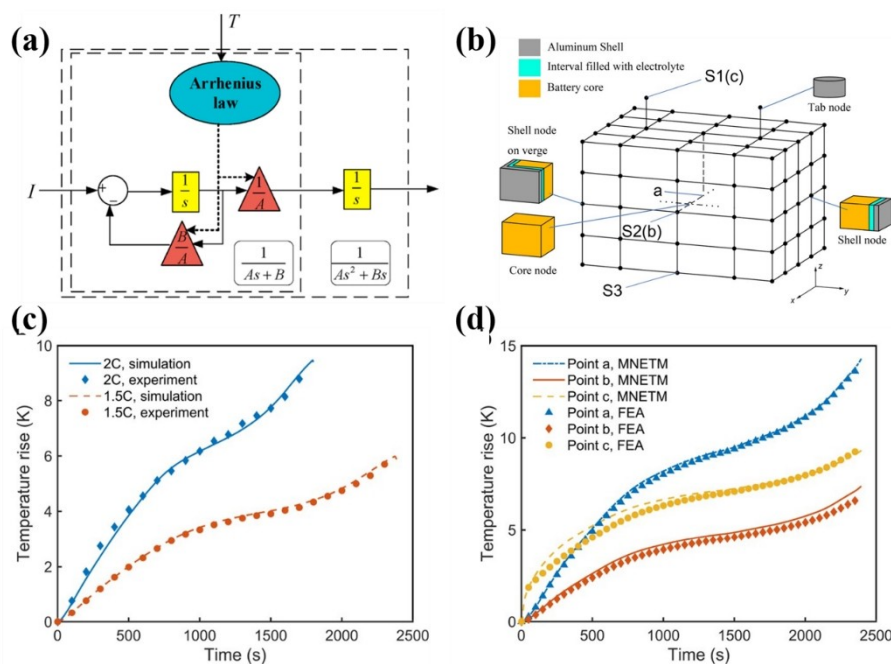
Figure 3. (a) Framework of temperature-dependent parameter extraction. A and B contain the temperature-dependent parameters. Adapted with permission from Ref. [44]. Copyright (2020) Elsevier. b) Multi-node heat transference model and the three types of nodes. (c) Results of the constant discharging tests. The comparison of simulated temperature rise and experimental data under different C-rate. (d) Comparison between FEA model and MNETM with different node numbers. Adapted with permission from Ref. [46]. Copyright (2020) Elsevier.

core structure of LIB, which describes the real-time temperature gradient inside the large prismatic LIB. The model includes two sub models: the heating model based on second-order ECM and the multi node heat transfer model based on battery geometry. Firstly, the ECM estimates the irreversible heat and calculates the reversible heat based on the input current and the battery SOC.

In addition, the heat generated by the battery is distributed to all nodes based on volume, so as to calculate the temperature distribution. Since the electrochemical process of LIB is very sensitive to temperature, the average temperature of the battery cell is fed back to the ECM to determine the model parameters. The schematic diagram of the model is shown in Figure 3(b). The effectiveness of the model is verified by taking 105 Ah prismatic battery as the research object. Figure 3(c) shows the comparison between simulation results (lines) and experimental data (points) at different C-rates. It can be seen that the thermal behavior of the battery is well captured. By comparing with fine element analysis (FEA) (FEA based methods can usually achieve very high accuracy, but the complexity of the model greatly limits its real-time application), which is in good agreement with FEA(as shown in Figure 3(d).

2.3.3. Thermal-Electricity-Aging Coupled Model

During the usage of LIBs, the decline of whole batteries is inevitable and depends on many factors, such as capacity/power decrease, internal resistance increase, working voltage drop, and self-discharge.[47] Tracking the aging phenomenon

can predict the remaining life of the battery and strengthen the health management. Therefore, it is essential to study the coupling model considering aging to evaluate and improve the life of power LIBs in EVs.

Gao et al.[48] designed a fast perceptional safe charging strategy of LIB based on the electrochemical-thermal-aging model. Charging time and battery capacity attenuation are affected by thermal constraints and degradation constraints. A maximum value of overpotential is utilized to prevent the battery from being overcharged by harsh currents. The health perceptional fast charging strategy under different currents is compared with minimum time charging and traditional constant-current/constant-voltage (CCCV) charging. The results show that at current densities of $I_{max} = 1$ C/2 C/3 C, the minimum charging time are 3082, 1959, and 2041 s, respectively, which is nearly 50% shorter than the CCCV at the same maximum current. When $I_{max} = 1$ C/2 C/3 C, the charging time of health-aware quick charging is 4961, 4200, and 3777 s, respectively. Although the charging time is longer than the minimum charging time, the degradation process of the battery is hugely alleviated.

Tran et al.[49] proposed a one-dimensional radial coupled degradation electrochemical thermal (DET) model for large-scale cylindrical LIBs. The model consists of a reduced order equation describing electrochemical phenomena (including electrochemical degradation) and an approximate model of thermal behavior, considering the filling of central electrolyte and hollow core. When simulating the time-varying temperature and gradient distribution in the battery, the proposed DET model has high computational efficiency while maintain-

Batteries & Supercaps

Review
doi.org/10.1002/batt.202100292

Chemistry
Europe
European Chemical
Societies Publishing

ing high accuracy (especially compared with the accuracy obtained using P2D model). The novelty of the model is that it is suitable for large scale cylindrical batteries and considers the non-uniform degradation and the thermal behavior coupled with electrochemical phenomena.

2.3.4. Thermo-Electric-Mechanical Coupled Model

Different parts of LIBs have different mechanical properties. Firstly, the separator has elastic-viscoplastic and temperature-related mechanical properties. Secondary, the collector is rate-dependent. Besides, continuous extraction and insertion of lithium ions into positively active material particles during charging and discharging will cause changes in electrode volume and accumulation of mechanical stress in the battery. When pressure builds up to a certain point, the integrity of electrodes may be broken, reducing the battery's durability.[50] Therefore, adding automated stress analysis is necessary for LIB modeling.

He et al.[51] revealed the related structure and chemical evolution of Si and SEI by integrating EDS tomography, cryogenic scanning transmission electron microscopy. It is found that the SEI gradually grows into Si, which makes Si nanowires become porous during cycling. Through their verification on chemical mechanism, it is proved that the electrolyte gradually infiltrates into porous Si nanowires, induce SEI grows extensively along the percolation channel, thus break the integrity of Si nanowire nano- structure during the delithiation process. The phase field model corresponding to the cross-section image of Si nanowires, which employed two special modeling processes are shown in Figure 4.

Oh et al.[52] established a fully coupled multiphysics model of LIBs. The multi-physical model consists of three main parts: the coupled electrothermal model (ETM), the expansion model, and the force estimator. ETM uses the measured current and ambient temperature to estimate the battery's SOC and surface/core temperature. The expansion model calculates the total volumetric expansion ratio of the battery without constraint at the surface/core/ambient temperature provided by SOC and ETM. Force estimator can compute the LIB volume change caused by lithium intercalating, temperature variation, and side reaction caused by preload. Under different operating conditions for many experimental validations, the results show that the model can accurately predict the battery in different preloading and the surface temperature of the ambient temperature and battery volume change produced by the reaction.

3. Sensor-Based Methods

General BMS relies on monitoring external performance parameters such as voltage, current and temperature to estimate SOC, state of health (SOH), power state (SOP) and protect the battery. Traditional methods to ensure the safe operation of batteries in the required range and available power include expensive design of batteries. The embedded sensor with more information is used for battery condition monitoring. It can provide accurate SOC estimation and early problem indication to improve the SOH estimation of BMS.[53]

3.1. Electrochemical Quartz Crystal Microbalance (EQCM)

Quartz crystal microbalance with dissipation monitoring (QCM–D) is a very sensitive mass detector, which can perform mass measurement at the Nanogram level. QCM–D is combined with electrochemical technology to form electrochemical quartz crystal microbalance (EQCM–D). It can obtain mass information as well as the electrochemical information, which enjoys the superiority that other methods cannot compare.[54] EQCM–D produces two coupled output responses, resonant frequency f/n and resonant bandwidth W/n, or equivalently, dissipation factor $D = W/f_0$; The output response is a function of n; f_0 stands for the fundamental frequency. By fitting the appropriate acoustic load impedance model with the variation of experimental frequency and dissipation factor ($\triangle f/n$ and $\triangle D$
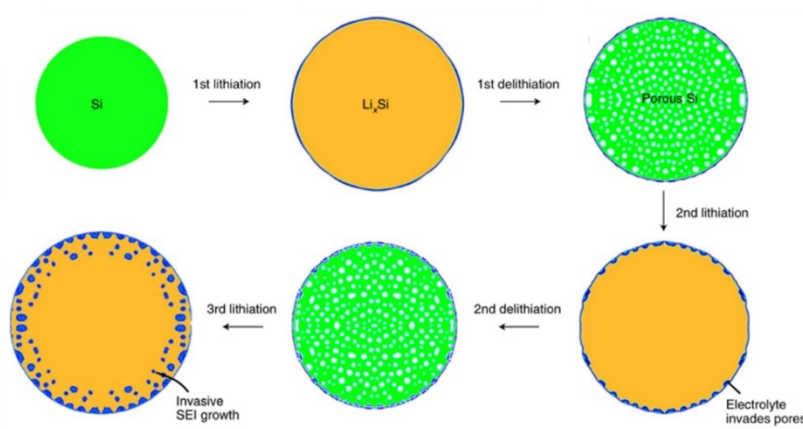

Figure 4. The mechanism diagram demonstrating structural collapse of silicon nanowire during lithiation/delithiation processes accompanied with the infiltration of electrolyte and reforming of SEI layers. Adapted with permission from Ref. [51]. Copyright (2021) The Author(s).

Batteries & Supercaps

Review
doi.org/10.1002/batt.202100292

Chemistry Europe
European Chemical
Societies Publishing

respectively), the viscoelastic change of the electrode is quantified.[54a,f,55] As shown in Figure 5(a, bottom), piezoelectric crystals generate surface acoustic waves in horizontal shear mode, penetrating thin electrode coatings in contact with gas or liquid. The load coating changes the F and W values of the original (uncoated) QC. Immersing the coating crystals in the liquid causes additional changes in F and W. Resonance frequency and the width of the resonance of the total displacement (Δf and ΔW) contains coded information about electrode material properties. Appropriate choice of thin electrode preparation and charging/cycling conditions, EQCM–D can be used as an electrode's in-situ probe, as shown in the top panel in Figure 5(a).

Shpigel et al.[56] used multi-harmonic EQCM–D to in situ evaluate the weight and viscoelastic changes of composite $Li_4Ti_5O_{12}$ (LTO) electrodes caused by simultaneous insertion/extraction of lithium ions and surface-generated/grown SEI in different lithium battery electrolyte solutions. LTO is considered a "zero stress" material, and the measured EQCM–D parameters can be attributed to the changes caused by the intercalation of the electrode and the combined changes in the weight and viscoelasticity of the resulting surface film. Three commonly used electrolyte solutions were selected: LiTFSI, LiPF$_6$, and LiPF$_6$ +2% VC in the EC-DMC solvent mixture. By using the theory of acoustic multilayer, formalism establishes the self-consistent viscoelastic model of the composite LTO electrode. They were describing the experimental resonance frequency and resonance width changes in gas/air environment, electrolyte contact with lithium battery, and applied potential. The main

finding is that EQCM–D can initially screen out lithium battery electrolytes and additives in short-term experiments. The CV of the LTO electrode in LiTFSI and LiPF$_6$ solutions are shown in Figure 5(b and c). The use of a viscoelastic model to quantify the mechanical parameters of the generated SEI shows that compared with other electrolyte solutions, the quality of the SEI formed on the LTO anode in the LiTFSI solution is higher, expressed by the most top storage modulus and lowest thickness (Figure 5d and e).

In order to study the changes of porous electrode structure caused by lithium ion embedding on the mesoscopic scale, Dargel and Shpigel et al.[54c] used EQCM–D technology to characterize the size and viscoelastic changes of $Li_2Mn_2O_4$ electrode material in real LIB. The quartz crystal surface during detection is shown in Figure 5(f). In their experiment, the $Li_2Mn_2O_4$ coating was first formed on the quartz crystal surface by spray pyrolysis method. After the preparation process, the quality of the coating was calculated by measuring the frequency difference. The frequency change Δf and formant width ΔW are normalized by overtone orders n, and the linear relationship between them and the penetration depth δ_n of resonant wave in the electrode is obtained. The structural parameters such as the average thickness of hydrodynamic porous boundary layer and the penetration length of porous boundary layer are also calculated (Figure 5f). shows the electrode vibration dissipation in two cases. When the pore diameter is small, the electrolyte is "captured" by the porous system, and its moving speed is equal to the that of the crystal surface, thus showing a non-dissipative state; However, when
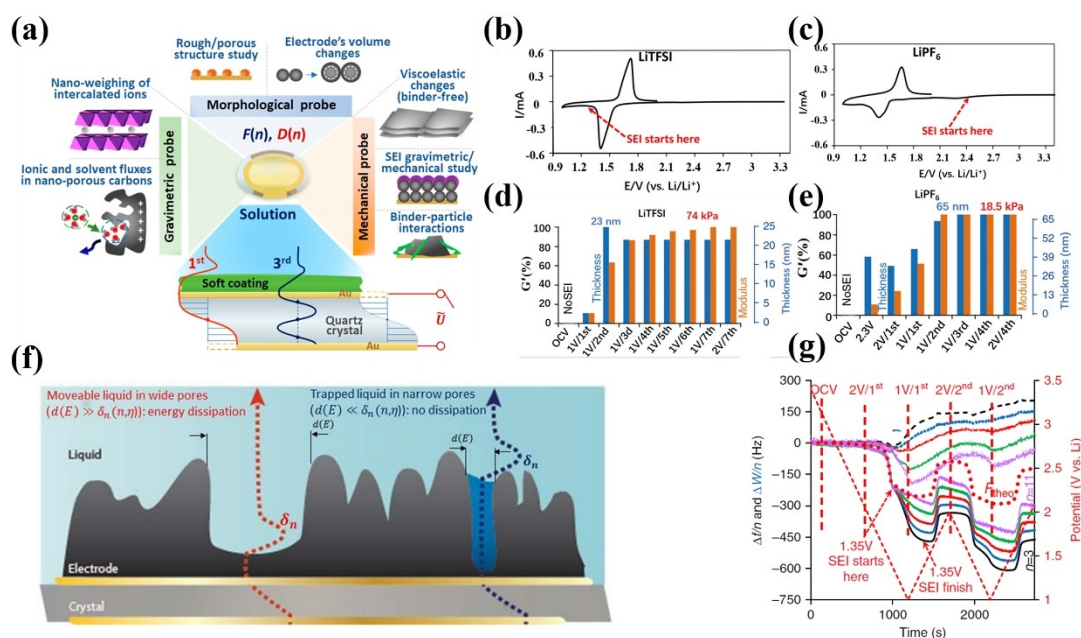

Figure 5. (a) EQCM–D is applied in the characterization of energy storage electrodes. In EC+DMC solution, the characteristics of composite LTO electrode in LiTFSI and LiPF$_6$ solution: the first few cycles (b, c, respectively). A diagram for calculating viscoelastic parameters (d, e, respectively). Adapted with permission from Ref. [56]. Copyright (2018) American Chemical Society. (f) Schematic diagram of the rough and porous electrode coating on the surface of the oscillating quartz crystal in contact with the electrolyte solution. Adapted with permission from Ref. [54c]. Copyright (2016) Nature Publishing Group. (g) Periodic changes in the vibration frequency and half-width of the quartz crystal during the first and second cycles of the battery. Adapted with permission from Ref. [57]. Copyright (2017) The Author(s).

Batteries & Supercaps

Review
doi.org/10.1002/batt.202100292

Chemistry Europe
European Chemical
Societies Publishing

the pore size is large, the electrolyte can move freely in the pore channel, resulting in the dissipation of vibration wave.

Subsequently, the research group also used EQCM–D technology to in-situ detect the SEI layer formation process of $Li_4Ti_5O_{12}$ electrode during lithium ion embedding.[57] In this experiment, the $Li–Li_4Ti_5O_{12}$ battery system using LiTFSI, $LiPF_6$ and $LiPF_6 + 2\%$ vinyl carbonate solution as electrolyte was chosen and the structural parameters of SEI layer were fitted by multi-layer viscoelastic model. Figure 5(g) shows the change of frequency and half peak width of quartz crystal with time under different harmonic orders n in the first two electrochemical cycles. It can be observed at the beginning and end of SEI layer formation process, $\Delta f/n$ and $\Delta W/n$ have changed obviously, and the change trend is similar to the theoretical prediction (F_{theo}, dotted line in the figure) calculated according to Sauerbrey formula.

3.2. Multi-Beam Optical Stress Sensor (MOSS)

Since the introduction of MOSS in 1996, the film stress measurement has been widely concerned.[58] MOSS is a very reliable in-situ measurement system that can determine changes in film stress through real-time curvature measurement.[59] It measures surface curvature by parallel laser beam arrays and charge-coupled device (CCD) area detectors.[60] The experimental schematic diagram is shown in Figure 6(a). Etalon is a highly reflective optical element, through which it can form a linear array of multiple beams. The numerous rays striking the specimen are parallel and of nearly uniform intensity. The corresponding reflected beam imaged on the CCD detector. The detector converts optical signals into

electrical signals picked up by a computer. The stress accuracy of the specimen is related to the beam spacing.[61]

The MOSS method is used for the first time to observe the stress evolution of silicon anodes during electrochemical lithiation and delithiation. This method can estimate the mechanical loss, modulus, and potential of silicon anodes.[62] The automatic dissolution of the silicon film electrode is equivalent to the polarization loss during lithiation.[62b] The elastic modulus of the Si anode is not a constant but a function of Li concentration,[62a] and the ratio of measured potential change to stress change was within the range of 100–125 mV/GPa, which proved the existence of stress-potential dependence in the lithiated-Si system.[63]

Although the traditional MOSS method can directly obtain the stress in the film, there are still some problems in the accuracy of stress. In order to improve the accuracy of stress detection, Chen et al.[64] proposed an in-situ method to simultaneously measure the real thickness and curvature of Li_xSi film during electrochemical cycle. The color evolution of silicon film is observed by optical microscope, and the real thickness is extracted directly from the relationship between color and film thickness. At the same time, the curvature of silicon electrode substrate was measured by MOSS method during electrochemical cycle. Finally, the exact stress of Li_xSi film during electrochemical cycle can be obtained by replacing the curvature and thickness data with Stoney equation. The advantage of this method is that the curvature and color evolution can be obtained simultaneously, while the thickness evolution is obtained by colorimetry. In the past, the thickness was calculated by capacity, which was easily affected by the electrochemical environment.
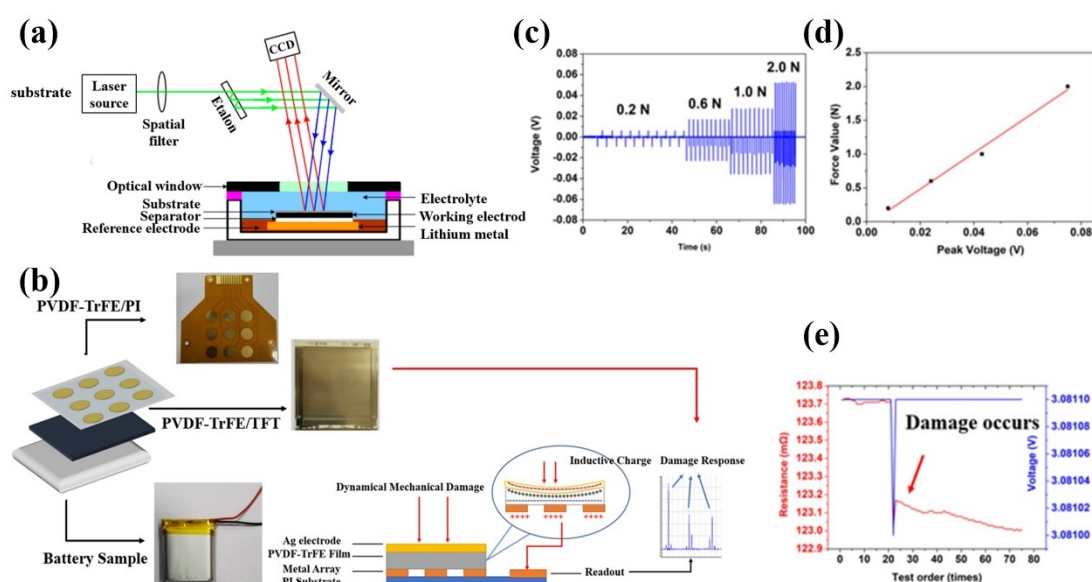

Figure 6. (a) MOSS experimental setup. Adapted with permission from Ref. [61]. Copyright (2017) The Author(s). (b) Structure and response principle to the dynamical mechanical damage of LBHMAS, (c) response signal to the puncture damage of LBHMAS, (d) linear relationship between the response signal and the rotation speed of the motor, (e) the variation in the internal resistance and voltage of the battery sample before and after the puncture damage occurs. Adapted with permission from Ref. [13a]. Copyright (2020) Elsevier.

Batteries & Supercaps

Review

doi.org/10.1002/batt.202100292

Chemistry Europe
European Chemical
Societies Publishing

In addition to Si electrodes, the MOSS technique also investigated the effects of grain orientation, wetting process, C-rate, lithium-ion concentration, and SEI formation on the graphite-based anode and cathode stress. Mukhopadhyay et al.[65] used MOSS to study the effect of graphene layer orientation on the stress evolution of carbon thin film electrodes. Sethuraman et al. and Nadimpalli et al.[66] studied the stress evolution of a dry graphite anode or nickel cobalt manganese (NMC) cathode immersed in an electrolyte, respectively. The electrode stress is not only caused by the concentration of Li-ion but also affected by the rate of charge and discharge rate. Through the stress growth of different thickness electrodes, Mukhopadhyay et al. believed that the irreversible stress of graphite electrodes was mainly related to the formation of the SEI layer in the first cycle, which was also confirmed by chemical vapor deposition.[60,67]

3.3. Piezo-Pyroelectric Thin Film Sensor

Piezoelectric material refers to the charge that can spontaneously generate linearly related to the external force under the stimulation of external force and convert the external stimulation into electrical signal.[68] Pyroelectric material is a dielectric with spontaneous polarization characteristics. In general, the surface bound charge generated by the spontaneous polarization of the crystal is shielded by the free charge adsorbed on the crystal surface. When the temperature changes, the spontaneous polarization changes, thus releasing part of the charge adsorbed on the surface. When the crystal is cooled, the charge polarity is opposite to that when it is heated. Pyroelectric materials are a kind of piezoelectric materials.[69]

Hu et al.[13a] prepared a new LIB in-situ health monitoring sensor array using piezoelectric material polyvinylidene fluoride (PVDF), pyroelectric material polytrifluoroethylene (TrFE) and in-situ polarized thin film transistor array (TFT). Piezoelectric/pyroelectric sensors can realize real-time response to dynamic mechanical damage and thermal damage by detecting electrical signals converted from dynamic mechanical damage (such as falling, collision, puncture) or thermal damage. However, due to the limited induced charge generated by limited crystal deformation, the sensitivity of piezoelectric/pyroelectric materials to quasi-static mechanical damage (expansion damage) is still limited on low degree. Therefore, dielectric materials can achieve a sensitive response to quasi-static mechanical signals through capacitance changes. However, dielectric materials are usually less sensitive to dynamic mechanical and thermal signals. Therefore, the combination of piezoelectric/pyroelectric and dielectric materials can be used to develop integrated sensors that can realize real-time health monitoring of LIB. In order to study the dynamic mechanical damage of the battery, a linear motor is used to simulate the puncture damage of the LIB. The linear motor has a tip and periodically impacts the battery sample, as shown in Figure 6(b). Figure 6(c) provides the signal of the sensor in response to puncture injury, showing a periodic piezoelectric pulse voltage response. As shown in Figure 6(d), the piezoelectric pulse voltage increases linearly with the increase of force value of the applied puncture damage, indicating that the sensor can respond to different puncture values in real time. In addition, according to the linear relationship between the force value and the piezoelectric pulse voltage, the degree of battery damage can be inferred from the voltage value, which is helpful to evaluate the health state of the battery. Figure 6(e) shows the output voltage and internal resistance before and after breakdown damage. Before the application of puncture injury, the output voltage and internal resistance are constant, while after the application of puncture injury, the output voltage becomes zero and the internal resistance becomes infinite. This phenomenon indicates that the battery sample has been seriously and irreversibly damaged. In addition, the integrated sensor also realizes the real-time detection of battery thermal damage and expansion damage.

3.4. Thin-Film Thermocouples Sensor (TFTCs)

TFTCs has the advantages of small size and fast response. The typical TFTC is tens of micrometers in size and has a response time of less than one microsecond, which is significantly better than traditional temperature sensors.[70] Mutyala et al.[71] proposed a novel thin-film sensor transfer technology to overcome the difficulty of directly preparing multilayer thin-film sensors on rough, flexible metal substrates. K-type TFTCs encapsulated with polyimide were made on a glass substrate by traditional micromachining technology. Then the sensor film was stripped from the substrate and then connected to the copper collector of the battery. The insertion of the sensor into the cell is done in a semi-automated manner, adding only one step to an existing battery assembly line, and is therefore robust and repeatable. Compared with other methods reported in the literature, this method does not require battery replacement or damage, and the geometry of the sensor can be customized according to the shape of the existing pouch battery.

The TFTC inside the battery can reliably measure the temperature change of the cell, and the temperature difference with the reference TC is tiny. Besides, there are no adverse effects such as electrolyte leakage, battery inflation, internal short circuit, drying, and plate corrosion during the battery assembly.

3.5. Fiber Optical Sensor

Fiber optic sensors have the advantages of small size, high flexibility, and the ability to monitor multiple points on the same optical fiber at the same time. They are widely used for temperature, pressure, and strain measurement inside batteries.[72] The most commonly used material of optical fiber sensor is silicon, which is corrosion-resistant. It can withstand tensile pressure of up to 1 GPa for a long time, dielectric breakdown length is greater than 470 kV/mm, and can work

between -200–$800\,°C$. All these characteristics make it an attractive and promising sensor embedded in LIB.[73]

Raghavan et al.[53a,74] monitored the internal stress and temperature of the battery based on the monitoring device of embedded fiber Bragg grating (FBG) sensor and estimated the SOC state of the battery. Nascimento et al.[75] proposed an internal temperature detection method of LIB coupled by FBG sensor and Fabry-Perot, and then subtracted the internal strain signal detected by Fabry-Perot from the signal detected by FBG sensor to obtain the accurate internal temperature of LIB.

Huang et al.[14] used the traditional single-mode or micron fiber Bragg grating (FBG) sensor to equip the battery with optical sensing function, and successfully unlocked the high-precision on-line monitoring of temperature and pressure during their cycling. Figure 7(a) shows the scheme of FBG sensor and its working principle: the sensor acts as a reflector for a specific wavelength, which is defined by $\lambda_B = 2n_{eff}\Lambda$ (where λ_B is the Bragg wavelength, n_{eff} is the effective refractive index of the grating and Λ is the Bragg grating period). This typical measurement consists of monitoring wavelength shifts of the reflected peak ($\Delta\lambda_B$), which results from changes in n_{eff} and Λ, both of which depend on local temperature (T), pressure (P) and strain (ε) changes. By adjusting the fiber morphology and the wavelength related to temperature and pressure, the chemical changes in the battery cycle can be accurately spotted, the temperature and pressure distributions generated by the first charge and discharge are demonstrated in Figure 7(b). During the first charging process, the time evolution of the internal temperature $\triangle T$ shows four peaks (expressed as i_c, ii_c, iii_c and iv_c), of which only two persist in the subsequent discharge (iii_d and iv_d). In addition, the peak ii_c of the maximum amplitude in the first charge completely disappears in the second charge, while $\triangle P$ rises sharply, indicating the gas generation. In the subsequent cycle, the exist of both characteristics also indicates an irreversibility which is consistent with SEI growing as well. In addition, the author also demonstrates how to use multiple sensors to monitor the heat generated by the

battery without using microcalorimetry. Different from other traditional isothermal calorimetry, the thermal capacity contribution of the battery can be easily evaluated by FBG, allowing a fully parameterized thermal modeling. These findings provide a scalable solution for screening electrolyte additives, quick SEI identification for most commercial battery systems and matched thermal management systems.

4. Summary

In this paper, several state-of-the-art portable *in situ* monitoring methods of safety batteries in recent years are reviewed, with emphasis on model-based methods and sensor methods. According to the discussion and systematic comparison, some typical modeling strategies, such as thermal modeling, EC modeling and coupling modeling studies related to LIBs security are introduced in depth. The thermal model alone is usually not enough to accurately predict the thermal behavior of the battery. Therefore, the thermal model is mostly coupled with the electrical model for modeling. When combined with the ECM, it is mainly used in the management system of electric vehicles.

In contrast, when coupled with the electrochemical model, it is more common in the study of internal battery characteristics. At the same time, the model based on the effect of aging and mechanical stress is more careful and realistic consideration for the battery, and also a requirement for the future development of battery modeling technology. In brief, modeling plays a critical role in the development of LIB and opens the horizon to more technological advances. The use of additional information sensors to monitor internal battery status provides an early fault indicator is critical for effective control of the BMS. Accompanied by the accelerated promotion of EVs and other large electric devices in the future, the miniaturization of battery health monitoring will attract more attention.
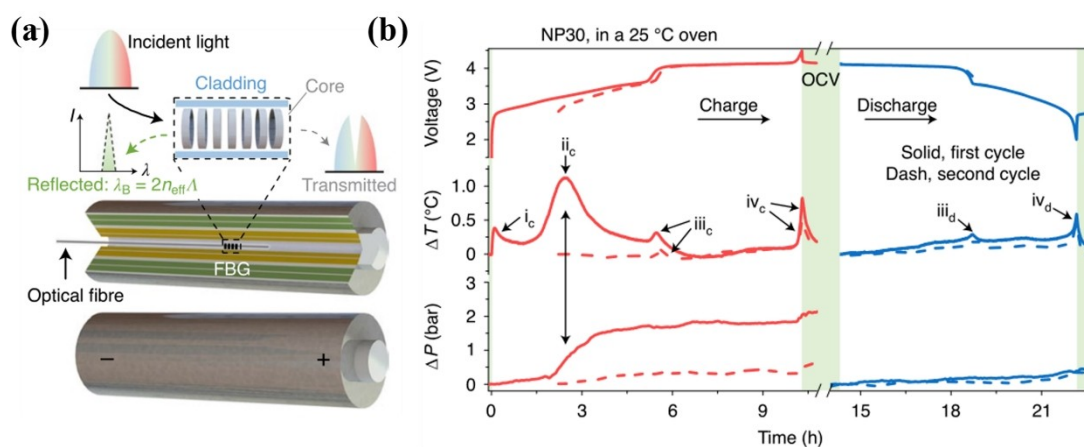

Figure 7. (a) The scheme of FBG sensor and its working principle. (b) The temporal voltage (top), internal temperature change (middle) and pressure change (bottom) during the first (solid curves) and second (dashed curves) charge/discharge of NVPF/HC at C/10 and 25 °C with ethylene carbonate-dimethyl carbonate (NP30). Adapted with permission from Ref. [14]. Copyright (2020) The Author(s).

Batteries & Supercaps

Review
doi.org/10.1002/batt.202100292

Chemistry Europe
European Chemical
Societies Publishing

Declaration of competing interest

The authors declare that they have no known competing financial interests or personal relationships that could have appeared to influence the work reported in this paper.

Acknowledgements

Conflict of Interest

The authors declare no conflict of interest.

[1] a) A. Fotouhi, D. J. Auger, K. Propp, S. Longo, M. Wild, *Renewable Sustainable Energy Rev.* **2016**, *56*, 1008–1021; b) M. U. Ali, S. H. Nengroo, M. A. Khan, K. Zeb, M. A. Kamran, H. J. Kim, *Energies* **2018**, *11*, 1122 ; c) K. L. Liu, K. Li, Q. Peng, C. Zhang, *Frontiers of Mechanical Engineering* **2019**, *14*, 47–64; d) J. Guo, G. Zhao, T. Xie, D. Dong, C. Ma, L. Su, L. Gong, X. Lou, X. Guo, J. Wang, Y. Zhu, *ACS Appl. Mater. Interfaces* **2020**, *12*, 19023–19032.

[2] Z. H. Liao, S. Zhang, K. Li, G. Q. Zhang, T. G. Habetler, *J. Power Sources* **2019**, *436*, 226879.

[3] a) W. Hong, A. Wang, L. Li, T. Qiu, J. Li, Y. Jiang, G. Zou, H. Peng, H. Hou, X. Ji, *Adv. Funct. Mater.* **2020**, *31*, 2000756; b) M. M. Rahman, S. Mateti, Q. Cai, I. Sultana, Y. Fan, X. Wang, C. Hou, Y. Chen, *Energy Storage Mater.* **2019**, *19*, 352–359; c) R. Xu, F. Han, X. Ji, X. Fan, J. Tu, C. Wang, *Nano Energy* **2018**, *53*, 958–966; d) S. Abada, M. Petit, A. Lecocq, G. Marlair, V. Sauvant-Moynot, F. Huet, *J. Power Sources* **2018**, *399*, 264–273.

[4] a) Q. F. Cai, J. Wang, Y. C. Jiao, T. T. Li, Y. Xia, M. Z. Li, Y. C. Yang, G. H. Wu, J. X. Zou, J. H. Hu, A. G. Dong, D. Yang, *Small* **2021**, *17*, 2101173; b) C. Gong, S. D. D. Pu, X. W. Gao, S. X. Yang, J. L. Liu, Z. Y. Ning, G. J. Rees, I. Capone, L. Q. Pi, B. Y. Liu, G. O. Hartley, J. Fawdon, J. Luo, M. Pasta, C. R. M. Grovenor, P. G. Bruce, A. W. Robertson, *Adv. Energy Mater.* **2021**, *11*, 2003118; c) S. Ha, J. C. Hyun, J. H. Kwak, H. D. Lim, Y. S. Yun, *Small* **2020**, *16*, 2003918.

[5] G. L. Hou, B. L. Cheng, Y. J. Yang, Y. Du, Y. H. Zhang, B. Q. Li, J. P. He, Y. Z. Zhou, D. Yi, N. N. Zhao, Y. Bando, D. Golberg, J. N. Yao, X. Wang, F. L. Yuan, *ACS Nano* **2019**, *13*, 10179–10190.

[6] Q. P. Wu, Y. J. Zheng, X. Guan, J. Xu, F. H. Cao, C. L. Li, *Adv. Funct. Mater.* **2021**, *31*, 2101034.

[7] a) C. Y. Lee, S. J. Lee, K. T. Yang, Y. M. Lee, M. S. Tang, P. C. Chen, Y. M. Chang, *Int. J. Green Energy* **2013**, *10*, 337–347; b) C. Y. Lee, S. J. Lee, M. S. Tang, P. C. Chen, *Sensors* **2011**, *11*, 9942–9950.

[8] D. Chen, S. Indris, M. Schulz, B. Gamer, R. Monig, *J. Power Sources* **2011**, *196*, 6382–6387.

[9] a) C. Y. Tang, S. J. Dillon, *J. Electrochem. Soc.* **2016**, *163*, A1660–A1665; b) X. Chen, J. Q. Lai, Y. B. Shen, Q. Chen, L. W. Chen, *Adv. Mater.* **2018**, *30*, 1802490.

[10] A. Stoddart, *Nat. Rev. Mater.* **2020**, *5*, 257–257.

[11] a) X. M. Li, Y. S. Li, Y. F. Tang, L. Q. Zhang, J. Y. Huang, *J. Power Sources* **2021**, *496*, 229868; b) Y. S. Li, Y. F. Tang, X. M. Li, W. Tu, L. Q. Zhang, J. Y. Huang, *Small* **2021**, *17*, 2100846.

[12] a) Y. Y. Li, C. Z. Ou, J. L. Zhu, Z. G. Liu, J. L. Yu, W. W. Li, H. Y. Zhang, Q. B. Zhang, Z. P. Guo, *Nano Lett.* **2020**, *20*, 2034–2046; b) C. Shen, S. Wang, Y. Jin, W. Q. Han, *ACS Appl. Mater. Interfaces* **2015**, *7*, 25441–7; c) C.-Y. Huang, Y.-T. Tseng, H.-Y. Lo, J.-K. Chang, W.-W. Wu, *Nano Energy* **2020**,

[13] *71*, 104625; d) Y. He, A. Zhou, D. Liu, Q. Hu, X. Liu, L. Wang, *ChemistrySelect* **2019**, *4*, 10694–10700.

[13] a) X. R. Hu, Z. L. Jiang, L. Q. Yan, G. T. Yang, J. Y. Xie, S. Liu, Q. Zhang, Y. Xiang, H. Min, X. L. Peng, *J. Power Sources* **2020**, *467*, 228367; b) T. H. Feng, L. Yang, X. W. Zhao, H. D. Zhang, J. X. Qiang, *J. Power Sources* **2015**, *281*, 192–203; c) P. D. Wang, X. Y. Zhang, L. Yang, X. Y. Zhang, M. Yang, H. S. Chen, D. N. Fang, *Extreme Mech. Lett.* **2016**, *9*, 459–466.

[14] J. Q. Huang, L. A. Blanquer, J. Bonefacino, E. R. Logan, D. A. Dalla Corte, C. Delacourt, B. M. Gallant, S. T. Boles, J. R. Dahn, H. Y. Tam, J. M. Tarascon, *Nat. Energy* **2020**, *5*, 674–683.

[15] The innovative technology of CATL. https://www.catl.com/en/research/technology/.

[16] G. L. Plett, *J. Power Sources* **2004**, *134*, 252–261.

[17] J. Zhang, X.-G. Yang, F. Sun, Z. Wang, C.-Y. Wang, *Appl. Energy* **2020**, *272*, 115262.

[18] K. Yan, J. Wang, S. Zhao, D. Zhou, B. Sun, Y. Cui, G. Wang, *Angew. Chem. Int. Ed.* **2019**, *58*, 11364–11368; *Angew. Chem.* **2019**, *131*, 11486–11490.

[19] D. T. Boyle, W. Huang, H. S. Wang, Y. Z. Li, H. Chen, Z. Yu, W. B. Zhang, Z. N. Bao, Y. Cui, *Nat. Energy* **2021**, *6*, 487–494.

[20] X. Y. Huang, M. Xiao, D. M. Han, J. J. Xue, S. J. Wang, Y. Z. Meng, *J. Power Sources* **2021**, *489*, 229503.

[21] K. Onda, T. Ohshima, M. Nakayama, K. Fukuda, T. Araki, *J. Power Sources* **2006**, *158*, 535–542.

[22] U. S. Kim, J. Yi, C. B. Shin, T. Han, S. Park, *J. Electrochem. Soc.* **2013**, *160*, A990-A995.

[23] S. L. Du, M. Jia, Y. Cheng, Y. W. Tang, H. L. Zhang, L. H. Ai, K. Zhang, Y. Q. Lai, *Int. J. Therm. Sci.* **2015**, *89*, 327–336.

[24] Y. Xie, W. Li, X. Hu, X. Lin, Y. Zhang, D. Dan, F. Feng, B. Liu, K. Li, *IEEE Trans. Transp. Electrif.* **2020**, *6*, 375–390.

[25] R. R. Richardson, S. Zhao, D. A. Howey, *J. Power Sources* **2016**, *326*, 377–388.

[26] X. F. Cui, J. Zeng, H. L. Zhang, J. H. Yang, J. Qiao, J. Li, W. X. Li, *J. Energy Storage* **2020**, *32*, 101758.

[27] M. Shen, Q. Gao, *Int. J. Energy Res.* **2019**, *43*, 5042–5075.

[28] a) V. Esfahanian, F. Chaychizadeh, H. Dehghandorost, H. Shokouhmand, *J. Electrochem. Soc.* **2019**, *166*, A1520–A1534; b) V. Laue, F. Röder, U. Krewer, *Electrochim. Acta* **2019**, *314*, 20–31.

[29] Q. Zhang, R. E. White, *J. Power Sources* **2008**, *179*, 793–798.

[30] K. Liu, K. Li, Q. Peng, C. Zhang, *Frontiers of Mechanical Engineering* **2019**, *14*, 47–64.

[31] a) S. Allu, S. Kalnaus, S. Simunovic, J. Nanda, J. A. Turner, S. Pannala, *J. Power Sources* **2016**, *325*, 42–50; b) J. Christensen, J. Newman, *J. Electrochem. Soc.* **2006**, *153*, A1019–A1030; c) M. Zhu, J. Park, A. M. Sastry, *J. Electrochem. Soc.* **2012**, *159*, A492–A498.

[32] Q. Zhang, Q. Z. Guo, R. E. White, *J. Power Sources* **2007**, *165*, 427–435.

[33] a) J. Li, Y. Cheng, M. Jia, Y. W. Tang, Y. Lin, Z. A. Zhang, Y. X. Liu, *J. Power Sources* **2014**, *255*, 130–143; b) S. F. Yuan, L. Jiang, C. L. Yin, H. J. Wu, X. Zhang, *J. Power Sources* **2017**, *352*, 245–257.

[34] K. Smith, C. Y. Wang, *J. Power Sources* **2006**, *161*, 628–639.

[35] a) S. Basu, K. S. Hariharan, S. M. Kolake, T. Song, D. K. Sohn, T. Yeo, *Appl. Energy* **2016**, *181*, 1–13; b) S. Basu, R. S. Patil, S. Ramachandran, K. S. Hariharan, S. M. Kolake, T. Song, D. Oh, T. Yeo, S. Doo, *J. Power Sources* **2015**, *283*, 132–150.

[36] C. Lyu, Y. Song, J. Zheng, W. Luo, G. Hinds, J. Li, L. Wang, *Appl. Energy* **2019**, *250*, 685–696.

[37] M. Hahn, A. Schiela, P. Mossle, F. Katzer, M. A. Danzer, *J. Power Sources* **2020**, *477*, 228672.

[38] a) H. W. He, R. Xiong, H. Q. Guo, *Appl. Energy* **2012**, *89*, 413–420; b) H. W. He, R. Xiong, J. X. Fan, *Energies* **2011**, *4*, 582–598; c) S. Nejad, D. T. Gladwin, D. A. Stone, *J. Power Sources* **2016**, *316*, 183–196.

[39] a) G. L. Plett, *J. Power Sources* **2004**, *134*, 262–276; b) G. L. Plett, *J. Power Sources* **2004**, *134*, 277–292.

[40] a) A. Seaman, T.-S. Dao, J. McPhee, *J. Power Sources* **2014**, *256*, 410–423; b) M. Soltani, S. H. Beheshti, *J. Energy Storage* **2021**, *34*, 102019.

[41] M. Y. Wu, L. L. Qin, G. Wu, *J. Energy Storage* **2021**, *39*, 102535.

[42] Z. Li, J. Huang, B. Y. Liaw, J. B. Zhang, *J. Power Sources* **2017**, *348*, 281–301.

[43] M. Farag, H. Sweity, M. Fleckenstein, S. Habibi, *J. Power Sources* **2017**, *360*, 618–633.

[44] Y. Gao, C. Zhu, X. Zhang, B. Guo, *Energy* **2021**, *221*, 119688.

[45] J. Jiang, H. Ruan, B. Sun, W. Zhang, W. Gao, L. Y. Wang, L. Zhang, *Appl. Energy* **2016**, *177*, 804–816.

[46] Y. W. Pan, Y. Hua, S. D. Zhou, R. He, Y. L. Zhang, S. C. Yang, X. H. Liu, Y. B. Lian, X. Y. Yan, B. Wu, *J. Power Sources* **2020**, *459*, 228070.

Batteries & Supercaps

Review

doi.org/10.1002/batt.202100292

Chemistry Europe

European Chemical
Societies Publishing

[47] a) P. Singh, N. Khare, P. K. Chaturvedi, *Eng. Sci. Technol.* **2018**, *21*, 35–42; b) T. L. Lu, Y. Luo, Y. X. Zhang, W. L. Luo, L. Q. Yan, J. Y. Xie, *J. Electrochem. Soc.* **2017**, *164*, A775–A784; c) J. G. Xu, R. D. Deshpande, J. Pan, Y. T. Cheng, V. S. Battaglia, *J. Electrochem. Soc.* **2015**, *162*, A2026–A2035; d) H. Karlsen, T. Dong, Z. C. Yang, R. Carvalho, *IEEE Access* **2019**, *7*, 142203–142213.

[48] Y. Z. Gao, X. Zhang, B. J. Guo, C. Zhu, J. Wiedemann, L. Wang, J. H. Cao, *IEEE Trans. Ind. Inform.* **2020**, *16*, 3417–3429.

[49] N. T. Tran, T. Farrell, M. Vilathgamuwa, S. Choi, Y. Li, *J. Electrochem. Soc.* **2019**, *166*, A3059–A3071.

[50] H. Jiang, Y. Hu, S. Guo, C. Yan, P. S. Lee, C. Li, *ACS Nano* **2014**, *8*, 6038–46.

[51] Y. He, L. Jiang, T. W. Chen, Y. B. Xu, H. P. Jia, R. Yi, D. C. Xue, M. Song, A. Genc, C. Bouchet-Marquis, L. Pullan, T. Tessner, J. Yoo, X. L. Li, J. G. Zhang, S. L. Zhang, C. M. Wang, *Nat. Nanotechnol.* **2021**, *16*, 1113–1120.

[52] K. Y. Oh, N. A. Samad, Y. Kim, J. B. Siegel, A. G. Stefanopoulou, B. I. Epureanu, *J. Power Sources* **2016**, *326*, 447–458.

[53] a) A. Raghavan, P. Kiesel, L. W. Sommer, J. Schwartz, A. Lochbaum, A. Hegyi, A. Schuh, K. Arakaki, B. Saha, A. Ganguli, K. H. Kim, C. Kim, H. J. Hah, S. Kim, G. O. Hwang, G. C. Chung, B. Choi, M. Alamgir, *J. Power Sources* **2017**, *341*, 466–473; b) J. Fleming, T. Amietszajew, J. Charmet, A. J. Roberts, D. Greenwood, R. Bhagat, *J. Energy Storage* **2019**, *22*, 36–43.

[54] a) M. D. Levi, N. Shpigel, S. Sigalov, V. Dargel, L. Daikhin, D. Aurbach, *Electrochim. Acta* **2017**, *232*, 271–284; b) N. Shpigel, S. Sigalov, M. D. Levi, T. Mathis, L. Daikhin, A. Janes, E. Lust, Y. Gogotsi, D. Aurbach, *Joule* **2018**, *2*, 988–1003; c) N. Shpigel, M. D. Levi, S. Sigalov, O. Girshevitz, D. Aurbach, L. Daikhin, P. Pikma, M. Marandi, A. Janes, E. Lust, N. Jackel, V. Presser, *Nat. Mater.* **2016**, *15*, 570–575; d) N. Shpigel, M. D. Levi, S. Sigalov, O. Girshevitz, D. Aurbach, L. Daikhin, P. Pikma, M. Marandi, A. Janes, E. Lust, N. Jackel, V. Presser, *Nat. Mater.* **2016**, *15*, 570–5; e) N. Shpigel, M. D. Levi, D. Aurbach, *Energy Storage Mater.* **2019**, *21*, 399–413; f) N. Shpigel, M. D. Levi, S. Sigalov, L. Daikhin, D. Aurbach, *Acc. Chem. Res.* **2018**, *51*, 69–79.

[55] a) M. D. Levi, L. Daikhin, D. Aurbach, V. Presser, *Electrochem. Commun.* **2016**, *67*, 16–21; b) S. Sigalov, N. Shpigel, M. D. Levi, M. Feldberg, L. Daikhin, D. Aurbach, *Anal. Chem.* **2016**, *88*, 10151–10157.

[56] N. Shpigel, M. D. Levi, S. Sigalov, L. Daikhin, D. Aurbach, *Acc. Chem. Res.* **2018**, *51*, 69–79.

[57] V. Dargel, N. Shpigel, S. Sigalov, P. Nayak, M. D. Levis, L. Daikhin, D. Aurbach, *Nat. Commun.* **2017**, *8*, 1389.

[58] a) J. B. Jiang, B. Kee, *Optik* **2003**, *114*, 427–432; b) J. B. Jiang, H. D. Hwang, H. S. Lee, B. J. Kim, K. Bong, E. J. Yoon, *J. Cryst. Growth* **2004**, *260*, 277–285.

[59] J. F. Geisz, A. X. Levander, A. G. Norman, K. M. Jones, M. J. Romero, *J. Cryst. Growth* **2008**, *310*, 2339–2344.

[60] A. Tokranov, B. W. Sheldon, P. Lu, X. Xiao, A. Mukhopadhyay, *J. Electrochem. Soc.* **2014**, *161*, A58–A65.

[61] X. M. Cheng, M. Pecht, *Energies* **2017**, *10*, 591.

[62] a) V. A. Sethuraman, M. J. Chon, M. Shimshak, N. Van Winkle, P. R. Guduru, *Electrochem. Commun.* **2010**, *12*, 1614–1617; b) V. A. Sethura-man, M. J. Chon, M. Shimshak, V. Srinivasan, P. R. Guduru, *J. Power Sources* **2010**, *195*, 5062–5066.

[63] V. A. Sethuraman, V. Srinivasan, A. F. Bower, P. R. Guduru, *J. Electrochem. Soc.* **2010**, *157*, A1253.

[64] J. Chen, L. Yang, Y. Han, Y. H. Bao, K. L. Zhang, X. Li, J. Pang, H. S. Chen, W. L. Song, Y. J. Wei, D. N. Fang, *J. Power Sources* **2019**, *444*, 227227.

[65] a) A. Mukhopadhyay, F. Guo, A. Tokranov, X. Xiao, R. H. Hurt, B. W. Sheldon, *Adv. Funct. Mater.* **2013**, *23*, 2397–2404; b) A. Mukhopadhyay, A. Tokranov, K. Sena, X. Xiao, B. W. Sheldon, *Carbon* **2011**, *49*, 2742–2749.

[66] a) V. A. Sethuraman, N. Van Winkle, D. P. Abraham, A. F. Bower, P. R. Guduru, *J. Power Sources* **2012**, *206*, 334–342; b) S. P. V. Nadimpalli, V. A. Sethuraman, D. P. Abraham, A. F. Bower, P. R. Guduru, *J. Electrochem. Soc.* **2015**, *162*, A2656–A2663.

[67] A. Mukhopadhyay, A. Tokranov, X. Xiao, B. W. Sheldon, *Electrochim. Acta* **2012**, *66*, 28–37.

[68] a) S. Trolier-McKinstry, S. Zhang, A. J. Bell, X. Tan, *Annu. Rev. Mater. Res.* **2018**, *48*, 191–217; b) H. Wei, H. Wang, Y. Xia, D. Cui, Y. Shi, M. Dong, C. Liu, T. Ding, J. Zhang, Y. Ma, N. Wang, Z. Wang, Y. Sun, R. Wei, Z. Guo, *J. Mater. Chem. C* **2018**, *6*, 12446–12467; c) A. Zaszczynska, A. Gradys, P. Sajkiewicz, *Polymer* **2020**, *12*, 2754.

[69] a) C. R. Bowen, J. Taylor, E. LeBoulbar, D. Zabek, A. Chauhan, R. Vaish, *Energy Environ. Sci.* **2014**, *7*, 3836–3856; b) H. He, X. Lu, E. Hanc, C. Chen, H. Zhang, L. Lu, *J. Mater. Chem. C* **2020**, *8*, 1494–1516; c) R. Takahashi, M. Lippmaa, *Jpn. J. Appl. Phys.* **2018**, *57*, 0902 A1; d) J. Wang, C. Hu, L. Shi, N. Tian, H. Huang, H. Ou, Y. Zhang, *J. Mater. Chem. A* **2021**, *9*, 12400–12432.

[70] J. Z. Zhao, H. Li, H. Choi, W. N. Cai, J. A. Abell, X. C. Li, *J. Manuf. Process.* **2013**, *15*, 136–140.

[71] M. S. K. Mutyala, J. Zhao, J. Li, H. Pan, C. Yuan, X. Li, *J. Power Sources* **2014**, *260*, 43–49.

[72] a) B. Rente, M. Fabian, M. Vidakovic, X. Liu, X. Li, K. Li, T. Sun, K. T. V. Grattan, *IEEE Sens. J.* **2021**, *21*, 1453–1460; b) Y. J. Ee, K. S. Tey, K. S. Lim, P. Shrivastava, S. B. R. S. Adnan, H. Ahmad, *J. Energy Storage* **2021**, *40*, 102704; c) J. Peng, S. H. Jia, Y. M. Jin, S. P. Xu, Z. D. Xu, *Sens. Actuators A Phys.* **2019**, *285*, 437–447.

[73] P. M. Nellen, P. Mauron, A. Frank, U. Sennhauser, K. Bohnert, P. Pequignot, P. Bodor, H. Brandle, *Sens. Actuators A Phys.* **2003**, *103*, 364–376.

[74] A. Ganguli, B. Saha, A. Raghavan, P. Kiesel, K. Arakaki, A. Schuh, J. Schwartz, A. Hegyi, L. W. Sommer, A. Lochbaum, S. Sahu, M. Alamgir, *J. Power Sources* **2017**, *341*, 474–482.

[75] M. Nascimento, S. Novais, M. S. Ding, M. S. Ferreira, S. Koch, S. Passerini, J. L. Pinto, *J. Power Sources* **2019**, *410*, 1–9.